

Deep generative computed perfusion-deficit mapping of ischaemic stroke

Chayanin Tangwiriyasakul^{1*}, Pedro Borges^{1**}, Guilherme Pombo^{2**}, Stefano Moriconi¹, Michael S. Elmalem², Paul Wright¹, Yee-Haur Mah³, Jane Rondina², Robert Gray², Sebastien Ourselin¹, Parashkev Nachev^{2***}, M. Jorge Cardoso^{1***}

1. School of Biomedical Engineering and Imaging Sciences, King's College London, London, SE1 7EU, UK

2. UCL Queen Square Institute of Neurology, University College London, London, WC1B 5EH, UK

3. King's College Hospital NHS Foundation Trust, Denmark Hill, London, SE5 9RS, UK

* This author is the corresponding author.

** These authors share second authorship.

*** These authors share senior authorship.

Abstract

Focal deficits in ischaemic stroke result from impaired perfusion downstream of a critical vascular occlusion. While parenchymal lesions are traditionally used to predict clinical deficits, the underlying pattern of disrupted perfusion provides information upstream of the lesion, potentially yielding earlier predictive and localizing signals. Such perfusion maps can be derived from routine CT angiography (CTA) widely deployed in clinical practice. Analysing computed perfusion maps from 1,393 CTA-imaged-patients with acute ischaemic stroke, we use deep generative inference to localise neural substrates of NIHSS sub-scores. We show that our approach replicates known lesion-deficit relations *without* knowledge of the lesion itself and reveals novel neural dependents. The high achieved anatomical fidelity suggests acute CTA-derived computed perfusion maps may be of substantial clinical-and-scientific value in rich phenotyping of acute stroke. Using only hyperacute imaging, deep generative inference could power highly expressive models of functional anatomical relations in ischaemic stroke within the pre-interventional window.

Introduction

Stroke is worldwide the second commonest cause of death and greatest cause of adult neurological disability¹, rendering even small improvements in its management of great value at the population level. Where its cause is vascular occlusion, the critical pathological process is hypoperfusion with resultant focal ischaemia. The complexity of the cerebrovascular architecture, in interaction with the occlusive mechanism, makes quantification of hypoperfusion challenging. We recently proposed a framework for deriving *computed perfusion maps* (CPM) from routine clinical CTA data². Our original work showed that CPM showed a high degree of spatial correlation (> 0.8) with the Time-to-maximum (T-max) map generated from RAPID-AI software analysis of perfusion imaging. Whereas RAPID-AI software requires a dedicated 4-dimensional CT (or MR) perfusion scan (4D-CTP), our CPM is derived directly from the routine CTA image, minimizing radiation exposure, lowering the barriers to clinical application, and permitting retrospective analysis of historical data.

Perfusion imaging is traditionally used to distinguish infarcted from merely threatened tissue for the purpose of treatment selection^{3,4}. But perfusion maps have potentially broader utility in capturing the anatomy of tissue under threat and relating it both to patient outcomes and the relationship between deficits and the underlying neural substrate. Our present study is concerned with illuminating the relation between CPMs and clinical deficits as captured by the NIHSS^{5,6}, through a novel method of functional anatomical inference—deep perfusion-deficit mapping—based on deep generative spatial inference previously validated in lesion-deficit mapping⁷.

The task of lesion-deficit inference requires a model with sufficient expressivity to capture both the topology of the neural substrate and the topology of the lesion-generating pathology. The assumption of no, or simple voxel, interdependence on which conventional mass-univariate approaches are based does not generally hold^{8,9}, and is manifestly violated in perfusion maps where complex spatial correlations inevitably reflect the complexity of the vascular tree. We need high-dimensional multivariate approaches capable of disentangling the anatomical features of a deficit's neural

dependence from those merely induced by the perfusion pattern. Recently, Pombo et al. proposed a deep variational autoencoder-based approach—DLM—for lesion-deficit mapping, based on deriving a joint latent representation of lesions and their associated deficits⁷, that in the largest and most comprehensive evaluation of its kind achieves substantially higher fidelity than alternative multivariate and mass-univariate approaches. In the present work, we extend DLM to the task of perfusion-deficit mapping in a large cohort of patients with ischaemic stroke (n=1393), inferring the functional anatomy of NIHSS sub-scores from CPMs derived from admission imaging.

Results

We present our results in six subsections clustered by broad behavioural domain: motor, consciousness, gaze and visual, language and articulation, somatosensory and attention (see Figs 3–8). Supplementary Figs 2–13 provide high-resolution grey and white matter maps for each NIHSS sub-score. Supplementary Fig 14 we summarised the critical tracts for all NIHSS scores, see details in the Supplementary Tables 1–12.

Motor substrates

Grey matter substrates showed strong lateralisation for both upper and lower limbs (Figs 3 & 4). In the upper limbs, right-sided impairments implicated contralateral middle frontal gyrus, insula, dorsal cingulate, anterior temporal cortex, occipital cortex, and midline and ipsilateral cerebellar regions. Left-sided impairments showed less extensive contralateral cortical associations involving the inferior parietal lobule, insula, and temporal pole, and cerebellar modulation was exclusively ipsilateral. There were no cortical areas of overlap, either supra- or infra-tentorially. In the lower limbs, right-sided impairments overlapped with the upper limb substrates with the exception of the dorsal cingulate, and additionally implicated inferior frontal gyrus, parietal cortex, and thalamus, as well as a region of the medial wall close to foot primary motor cortex. Left-sided impairments were similarly associated with more extensive substrates than in the upper limb, extending to contralateral middle frontal, and temporal cortices, as well as thalamus and ipsilateral occipital areas.

The affected WM tracts for the left hand and left leg showed clear contralateral lateralization, specifically involving the right uncinate fasciculus (UF_R), right dentatorubrothalamic tract (DRTT_R), right inferior fronto-occipital fasciculus (IFOF_R), and right medial lemniscus (ML_R). The WM tracts for the right hand and leg also exhibited lateralization, though less distinctly. Further details are available in Supplementary Figs 6–9.

Consciousness substrates

Loc-Question elicited predominantly left-sided GM substrates in the thalamus, insula, inferior and middle frontal gyrus, temporal lobe, inferior parietal lobule, and precuneus, as well as cerebellum and right-sided occipital areas (Fig 3). Loc-Command showed a similar pattern, but now involving left motor cortex, greater modulation of the left temporal lobe, a more ventral part of the precuneus, and right inferior frontal gyrus; thalamic and occipital substrates were not prominent. These patterns cohere with the differential demands on language and motor output of the task. No distinct substrates were identified with Loc-Arrival scores.

For both Loc-Question and Loc-Command, we observed strong left hemisphere lateralization of affected WM tracts. Nearly all affected bundles in Loc-Question were subsets of those in Loc-Command, specifically the left middle longitudinal fasciculus (MdLF_L) and left extreme capsule (EMC_L). Motor-related WM tracts, such as the left corticospinal tract (CST_L) and left dentatorubrothalamic tract (DRTT_L), appeared exclusively or showed greater disruption in Loc-Command than in Loc-Question. Further details are available in Supplementary Figs 3–4.

Gaze and Visual substrates

Strikingly, gaze elicited bilateral focal frontal and parietal regions closely corresponding to the established localizations of the frontal and parietal eye fields^{10,11} (Fig 6). Visual scores modulated occipital cortex and right inferior frontal regions. In patients with high gaze deficit scores, we observed a greater number of affected WM bundles, particularly in the right hemisphere, with the highest density in the right extreme capsule (EMC_R) and bilateral middle longitudinal fasciculus (MdLF). For visual scores, modest WM tract

disruption appeared in the left inferior longitudinal fasciculus (ILF_L) and right superior longitudinal fasciculus III (SLF3_R).

Language and Dysarthria substrates

Language scores robustly elicited a familiar left-lateralised network involving left inferior frontal, superior and middle temporal, and inferior parietal areas, as well as primary motor cortex, thalamus, precuneus, and cerebellum (Fig 7). Dysarthria modulated primary motor and inferior and middle frontal areas, and prominently cerebellum, with involvement of precuneus and other posterior regions.

Language deficits were associated predominantly with disrupted left extreme capsule (EMC_L) fibres, followed by the left corticopontine parietal tract (CPT_P_L) and the right extreme capsule (EMC_R). Additionally, both dentatorubrothalamic tracts (DRTT_L/R) showed impairment in both hemispheres. For dysarthria, the right extreme capsule (EMC_R) was most affected, followed by the right middle longitudinal fasciculus (MdLF_R) and then the left extreme capsule (EMC_L). Unlike in language deficits, only mild or no impairment was observed in the left and right dentatorubrothalamic tracts (DRTT_L/R), respectively. Disruption of the vermis tract (V) was elicited only by dysarthria.

Somatosensory and Attention substrates

Somatosensory scores, inevitably gated by linguistic ability, modulated right inferior frontal, superior temporal, and inferior parietal areas, as well as left occipitoparietal cortex (Fig 8). Attention, elicited a distributed, predominantly right-sided network, involving inferior frontal, temporal, parietal, and occipital areas, and including areas close to those modulated by gaze.

For somatosensory deficits, disrupted WM tracts were observed in both hemispheres, with a slight predominance in the right. The most affected bundles were the right extreme capsule (EMC_R) and right arcuate fasciculus (AF_R), followed by the right corticopontine parietal tract (CPT_P_R), superior longitudinal fasciculus III (SLF3_R), and medial lemniscus (ML_R). In patients with attentional deficits, disrupted WM bundles appeared in both hemispheres but were more prominent in the right. The top five affected bundles

were the right extreme capsule (EMC_R), right corticopontine frontal tract (CPT_F_R), right middle longitudinal fasciculus (MdLF_R), right corticobulbar tract (CBT_R), and right arcuate fasciculus (AF_R).

Other NIHSS scores

No substrates were identified for loc-arrival, facial palsy, ataxia scores.

Discussion

No investigational modality deployable in the acute setting provides a direct index of focal neural dysfunction. Structural imaging reveals tissue changes with largely speculative functional consequences; both BOLD and metabolic signals may be altered by microvascular rather than functional disruption. The neurophysiological impact of focal ischaemia must therefore be *inferred* from paired observations of anatomical maps of putatively threatened tissue and associated behavioural deficits. The complexities of the brain's functional neuroanatomy and vascular organization make such inference extraordinarily challenging, for the relation between intricate functional and vascular topologies is illuminated only by suboptimal lesion maps and crudely, reductively indexed behaviour. Crucially, high-resolution acute lesion maps are available exclusively from diffusion-weighted MR imaging that remains challenging to deploy in the clinical—especially hyperacute—setting, severely constraining the range, volume and inclusivity of the data to which models of necessarily high expressivity must be fitted.

Given an anatomical map of threatened tissue in a specific patient, we currently cannot confidently infer the dependence of the associated deficit on the observed topological characteristics, hindering prediction of both natural and interventional outcomes. Higher fidelity predictive models require either more informative imaging modalities^{12,13} or better analysis of existing signals. Though the former approach is theoretically superior, it is tightly constrained by the difficulty of introducing new modalities into clinical practice and by the time needed to obtain data of sufficient scale. Here we therefore focus on the latter, exploiting hitherto unrecognized signals in conventional CTA imaging with the aid of computational modelling.

Our approach requires a solution to two critical problems: extracting a tissue-level perfusion map from CTA, and inferring the neural substrate on which the behavioural consequences of impaired perfusion depend. We solve the former by using the anisotropy of the CTA image to derive perfusion maps with minimum prior assumptions on the structure of the underlying signal^{14,15}. This approach importantly does not involve any learnt, biological priors that could imperil generalisability beyond a specific training dataset, and involves comparatively few manipulable parameters. We solve the latter by adapting our deep variational lesion-deficit mapping method (DLM)⁷—demonstrated in the largest and most comprehensive evaluation to be substantially superior to all other widely used lesion-deficit methods—to inferring perfusion-deficit relations. DLM directly addresses the central problem of lesion-deficit mapping with vascular lesions: confounding by strong correlations across regions incidentally driven by the structure of the vascular tree.

Applied to a large cohort of patients with acute ischaemic stroke, these innovations enable us to reveal the neural substrates of the wide array of functional deficits captured by NIHSS sub-scores. For functions with well-defined substrates, such as language and gaze control, our results replicate known functional anatomy with surprising spatial precision, supporting the validity of computed perfusion, combined with DLM, as a functionally relevant measure of cerebral vascular integrity. Below we discuss the neuroanatomical findings, and examine the merits, demerits, and prospects of CTA-based perfusion-deficit mapping as a new tool for understanding the critical relation between focal cerebral ischaemia and its functional consequences.

The neural substrates of NIHSS

The interpretation of inferences to the neural substrates of NIHSS is complicated by the nature of the score and the context in which it is modelled. First, the NIHSS is not designed to isolate cognitive and behavioural functions that are both specific and orthogonal to each other, nor to account for dependencies between them. No simple score-based system could easily handle the censoring of one function by a deficit in another on which it depends, for example rule-following by dysphasia. It is therefore inevitable that the inferred neural substrates of a given subscore will extend to all the

functions invoked by the task, which may be common to several subscores. This is one important source of the well-known correlations between NIHSS subscores that substantially reduce the intrinsic dimensionality of the test^{16,17}. Second, as with lesion-deficit mapping in general, the inferred signals are necessarily contrastive against other lesioned patients rather than the normal state. Third, the spatial resolvability of a given substrate will jointly depend on the clinical eloquence of its disruption (i.e. the expressivity of the clinical deficit), the frequency with which it is lesioned, and the size of the lesions that involve it: eloquent substrates commonly affected by small lesions will be more sharply resolved than others.

Motor substrates

Clear lateralization—contralateral above the tentorium and ipsilateral below it—was evident across the four motor-related lesion maps, with more prominent modulation by right-sided deficits. Lateral cortical motor areas were revealed for right-sided deficits, including foot primary motor cortex medially; left-sided deficits induced a similar pattern that did not, however, cross the critical inferential threshold. Inferred WM pathways included corticopontine and dentatorubrothalamic tracts (DRTT) involved in movement generation¹⁸ and speculated to coordinate between the contralateral motor cortex and both ipsilateral¹⁹ and contralateral cerebellum²⁰. In contrast to Ferris et al., who found a correlation between motor impairment and the corticospinal (CST) damage²¹, we observed only moderately affected corticospinal tract involvement in the right leg WM map. Differences in laterality are potentially related to differences in clinical eloquence, including the association with language disturbance of left hemisphere lesions²².

Consciousness substrates

Loc-Question and Loc-Command sub-scores invoked left-sided substrates involved in the language processing^{23–25} necessary to perform these tasks. Thalamus and precuneus involvement was revealed in the former, in keeping with established evidence for the role of these areas in maintaining awareness^{26–29}. Greater thalamic activation in the Loc-Question map may underscore the difference between answering questions and following commands, with the thalamus more engaged in the former. Conversely, the motor cortical areas invoked by Loc-Command reflect the demand for movement

execution (such as “make a fist, open your hand”); similarly, PCC involvement is consistent with its role in visuomotor integration and executing complex tasks^{30,31}.

Across white matter substrates, both Loc-Question and Loc-Command showed clear left lateralization, likely due to the high language-processing demands of both tasks. The most affected tracts in Loc-Question included the left middle longitudinal fasciculus (MdLF_L)^{32,33}, left extreme capsule (EMC_L)^{34,35}, left acoustic radiation tract (AR_L)³⁶, and left inferior fronto-occipital fasciculus (IFOF_L)³⁷, each directly or indirectly facilitating language functions. In Loc-Command, these language-related tracts were also observed, along with additional WM tracts related to movement and motor control, such as the left corticopontine tract and left dentatorubrothalamic tract. Additionally, the left arcuate fasciculus (AF_L)³⁸, which connects Broca’s and Wernicke’s areas, and the left acoustic radiation (AR_L)³⁹ which transmits auditory information, were involved in both tasks, highlighting the essential role of language in each.

No neural dependents of Loc-Arrival were evident, potentially owing to inadequate sampling: 73.51% of our patients showed no deficit on this score, the second-highest rate after ataxia.

Gaze and Visual substrates

Visual subscores elicited left-sided occipital cortical substrates, but also right inferior frontal regions. Gaze scores, however, modulated remarkably circumscribed frontal and parietal areas closely corresponding to the known locations of the frontal and parietal eye fields^{10,40}. The absence of supplementary eye field substrates is plausibly explained by the comparative rarity of dorsomedial lesions and their modest impact on gaze^{41,42}. Other cortical areas, notably inferior frontal regions, precuneus, and cerebellum, fall within well-established networks involved in the control of gaze⁴³.

Modest modulation of white matter substrates by visual scores—the left inferior longitudinal fasciculus (ILF_L) and the right superior longitudinal fasciculus III (SLF3_R)—is consistent with sparse sampling of visual deficits. The ILF_L connects the occipital and temporal lobes, facilitating information transfer between these regions⁴⁴. SLF3_R is

another critical pathway for visuospatial information, linking the right parietal lobe to the right frontal lobe⁴⁵. Gaze modulated the right extreme capsule (EMC_R) and the left and right middle longitudinal fasciculi (MdLF_L and MdLF_R), in keeping with the role of these pathways in visuospatial and attentional processing^{46,47}.

Language and dysarthria substrates

Language sub-scores elicited known frontal and temporal cortical language areas, as well as thalamus, PCC, praecuneus, and midline cerebellum. Dysarthria substrates showed extensive cerebellar involvement alongside primary motor and inferior and middle frontal areas. A degree of overlap is expected given both tasks impose demands on language, though differing in emphasis. The language test (e.g., describing a picture) is a comparatively complex task requiring high-level semantic comprehension, in which the PCC⁴⁸, praecuneus⁴⁹ and thalamus⁵⁰ play critical roles. Note the less prominent temporo-parietal activation is predicted by the emphasis on expression (such as describing a picture) over comprehension in the language sub-score. The dysarthria task involves simply reading or repeating sentences, stressing higher-order aspects of linguistic ability to a lesser degree, which plausibly explains the lack of involvement of the thalamus, PCC, and praecuneus. Conversely, extensive cerebellar involvement is shown, consistent with dysarthria as a major manifestation of cerebellar dysfunction⁵¹.

The recruitment of the right frontal lobe seen in the dysarthria map may reflect compensatory mechanisms for cerebellar damage. A study by Geva et al. (2021) using fMRI found that patients with language deficits due to cerebellar damage showed greater activation in the right dorsal premotor cortex (r-PMd) and right supplementary motor area (r-SMA) compared to controls⁵². This compensation may involve recruiting intact brain areas, suggesting an indirect involvement of right motor-related brain areas in speech. Thus, the right motor-related lesions observed in our dysarthria map confirm their vital (though secondary to the cerebellum) roles in speech production.

For both language and dysarthria, we observed critical disruption in the left and right extreme capsule tracts (EMC_L/R). The left extreme capsule (EMC_L) connects Broca's and Wernicke's areas and is considered a vital component of the language pathway³⁴.

Although EMC_R does not traditionally play a primary role in language generation, a recent DTI study investigating the structural integrity of white matter tracts, including EMC_R, in individuals with primary progressive aphasia suggests a role for right-hemispheric WM, including EMC_R, in supporting language functions⁵³.

In addition to EMC_L/R, we found critical disruptions in the corticopontine parietal tract, particularly in the left hemisphere (CPT_P_L). Although CPT_P_L is not a core language tract, its role in motor planning and sensory integration may be essential for speech. Three key differences in tract involvement between language and dysarthria were identified: (1) the presence of the vermis tract, (2) the absence of DRTT_L/R, and (3) hemispheric asymmetry between MdLF_L and MdLF_R. These characteristics were uniquely observed in patients with dysarthria. Given its location within the cerebellum and its critical role in motor coordination⁵⁴ disruption of the vermis is expected in dysarthria patients.

In the language map, the disrupted dentatorubrothalamic tracts may reflect the high cognitive demands of the NIHSS language tasks, which require thalamic support (seen exclusively in the language GM map). This tract links the motor cortex, thalamus, caudate, and cerebellum¹⁸, underscoring its role in complex motor-cognitive integration.

Both left and right MdLF tracts play significant roles in language production³³. Similar to the GM map, greater disruption in MdLF_R compared to MdLF_L in dysarthria patients may indicate compensatory activation of right motor-related brain areas to offset cerebellar damage⁵², where MdLF_R is involved.

Somatosensory and attention substrates

The somatosensory cortical map primarily included right inferior frontal, superior temporal, and inferior parietal areas, as well as left occipitoparietal cortex. The marked right-sided lateralisation aligns with findings by Kessner et al.⁵⁵, whose somatosensorially affected cohort was heavily weighted on the right hemisphere.

Attention subscores elicited a predominantly right-sided frontoparietal network, consistent with both extant lesion and functional imaging data⁵⁶⁻⁵⁹. A degree of overlap with the inferred gaze network is predictable from putatively shared mechanisms for gaze and attentional shifts.

The prominent role of the insula in integrating multimodal sensory information⁶⁰ aligns with its appearance in both somatosensory and attention cortical maps. Other shared neural substrates between the somatosensory and attention maps include the right frontal and temporal lobes, which are critical for integrating somatosensory stimuli with cognitive attention networks. Lesions in these areas can lead to somatosensory deficits and neglect by disrupting both somatosensory processing and attentional allocation. Studies by Mort et al. and Dodds et al. have confirmed the importance of the right frontal and temporal lobes in both somatosensory and attention processing^{61,62}.

In the attention map, we also observed modulation of praecuneus, left cerebellum, and right occipital lobe. The praecuneus has been implicated in spatial cognition^{29,63,64}. A study of 80 stroke patients by Verdon et al. found an association between right occipital lesions and neglect⁶⁵ in keeping with our observations.

The exclusive left occipital lesion observed in the somatosensory GM map may reflect its secondary contribution to spatial awareness and integration with sensory information, although its primary function is visual. Lesions on the left occipital lobe may not directly cause tactile somatosensory loss but could disrupt visual-spatial integration, potentially affecting overall sensory awareness and spatial interpretation on the contralateral (right) side.

In both the somatosensory and attention maps, affected WM tracts were predominantly located in the right hemisphere. The five most affected tracts in the somatosensory map were the right extreme capsule (EMC_R), right arcuate fasciculus (AF_R), right corticopontine parietal tract (CPT_P_R), right superior longitudinal fasciculus III (SLF3_R), and right medial lemniscus (ML_R). For attention, the five most affected WM

tracts were EMC_R, CPT_P_R, the right middle longitudinal fasciculus (MdLF_R), bilateral corticobulbar tracts (CBT_L/R), and AF_R.

The EMC_R, AF_R, and CPT_P_R were common to both maps, in keeping with their joint association with sensory and attention networks³⁴. The arcuate fasciculus also plays an important role in orientation and attentional control due to its anatomical connections with the frontal, temporal, and parietal lobes, facilitating sensory integration and attentional processes^{38,45}. Lastly, the CPT_P_R connects the parietal cortical regions to the pons and brainstem, supporting sensory and motor integration and contributing to spatial awareness^{19,20}.

We identified SLF3_R and ML_R as somatosensory-specific tracts. SLF3_R is a white matter tract connecting the supramarginal gyrus and the inferior frontal gyrus, which supports its role in sensory processing, particularly proprioception⁶⁶. A DTI study by Chilvers et al. on 203 stroke survivors found that disconnections in white matter tracts, including SLF III, can lead to somatosensory deficits⁶⁷. ML_R is part of the dorsal column-medial lemniscus pathway, which is a sensory pathway in the central nervous system⁶⁸; thus, lesions in the ML_R tract could disrupt sensory information processing.

The MdLF, a white matter tract connecting the superior temporal gyrus to the posterior parietal cortex, appears in our attention map, in keeping with its role in spatial awareness and attention, particularly in processing verbal-auditory and spatial stimuli⁴⁷. Park et al. suggested that the corticobulbar tract, along with the extreme capsule, facilitates the integration necessary for visuomotor processing⁶⁹. Therefore, disruption of the corticobulbar tract could impact visuomotor orientation and spatial awareness, as observed in NIHSS attention deficits.

Negative sub-scores

No substrates were identified for Loc-Arrival, Facial Palsy, Ataxia sub-scores. The limited power reflects the low entropy of Ataxia and Loc-Arrival (see Supplementary Table 13). For Facial Palsy, an inferred GM substrate over the right frontal lobe was observed, aligning with Ding et al. and Onder et al.^{70,71}, although it was not statistically significant.

Deep perfusion-deficit mapping

The striking correspondence between inferred perfusion-deficit and known functional substrates strongly evidences the fidelity and expressivity of the proposed approach. Given the comparative crudity of NIHSS scores and the challenges of hyperacute imaging, the achieved performance is unlikely to be at its peak. We have deliberately left significant room for algorithmic optimisation of the computed perfusion map, eschewing learnt biological and pathological priors to eliminate trivial memorisation of neuroanatomical patterns during training. However, a correctly specified deep generative model of CPMs, given sufficient data, could enhance initial derivation by constraining the distribution of reconstructed perfusion patterns. Such a model could furthermore incorporate currently unmodelled instrumental parameters, such as the timing-and-phase of contrast administration. Equally, for the same reason the perfusion-deficit model excludes perfusion and functional-anatomical priors and can be extended to a semi-supervised framework utilising external data. That the simple approach here performs so well suggests that high-quality CTA-based perfusion-deficit inference is achievable, illuminating the critical relation between perfusion deficits and their functional consequences in the hyperacute setting.

We now consider SEVEN aspects of the method of relevance to its potential value.

First, the extraordinarily narrow pre-interventional window in stroke—ideally only a few minutes—renders infeasible the other widely available expressive modality, DWI. All extant lesion-deficit mapping studies in the acute setting^{70,72-74} use imaging conducted post-thrombolysis or thrombectomy, limiting inferences to the post-interventional state. Thus, differential neural susceptibility to treatment cannot be directly addressed at sufficient data scales or without bias.

Second, though dedicated CT-perfusion imaging optimised for microvascular signals is theoretically superior, it is unavailable at the data scale needed for sufficiently expressive perfusion-deficit models. While multimodal generative models of CTA and CTP could augment either modality, the critical limitation remains the volume of available paired behavioural data. Nonetheless, the tractability of perfusion-deficit inference may

promote wider prospective CTP use. Our approach remains the most applicable to large retrospective datasets.

Third, our focus is not merely quantifying perfusion or relating abnormalities to consequent lesions. Instead, it is on inferring the neural substrate underlying the perfusion-functional deficit relation, which perfusion alone or its correspondence with the final lesion cannot directly indicate. We do not compare computed perfusion abnormalities with CTP (evaluated elsewhere)² or with DWI: both are separate questions of independent interest, especially exploring intervention-induced differences. Our focus here is the perfusion-deficit relation, which is disclosed by paired imaging and behaviour.

Fourth, we aim not to predict individual patient deficits but to infer substrates across populations. Like all current lesion-deficit models, our approach assumes a shared underlying functional anatomy for any behavioural task. Revealing deficit-specific functional substrate distributions could enhance prediction, particularly treatment outcomes, by linking anatomically defined tissue threats with clinical outcomes. Inferred substrates could augment predictive and prescriptive models in observational and RCT settings^{75,76}.

Fifth, the discriminability of perfusion abnormalities varies with their size in complex ways. Small abnormalities may be concealed by noise; large abnormalities limit the spatial resolution of the inferred substrate. Additionally, vascular transit times vary across the brain⁷⁷, with effects on differential susceptibility to vascular insult that remain ill-defined. Any perfusion map, both computed and direct, is liable to resultant variations in fidelity across the brain and patterns of vascular occlusion.

Sixth, though CT is a quantitative modality, instrumental variability may limit generalisability across institutions. Not relying on highly expressive, learnt priors should mitigate the impact of instrumental variation, but future multicentre studies should explore this further.

Finally, perfusion-deficit inference inherits the considerable methodological challenges of lesion-deficit inference, for which only complex models with sufficient expressivity to capture the intricacies of functional and vascular anatomy could conceivably suffice^{9,78}. Disentangling functionally critical vs incidental pathological patterns is especially important where, as here, the pathology is spatially highly structured. Since this task lacks a ground truth, the fidelity of any method relies on large-scale semi-synthetic simulations of the kind that support our choice of architecture, shown in the most comprehensive published evaluation to exceed the preceding state-of-the-art by a substantial margin⁷. Nonetheless this remains an area of intense investigation.

Conclusion

We introduce a novel perfusion-deficit mapping method combining CTA-derived computed perfusion maps with deep generative topological inference. We validate our approach on a large cohort of patients with acute ischaemic stroke imaged with CTA and assessed on the NIHSS. Inferred substrates across grey and white matter correspond closely to known functional anatomy, while revealing potentially new functional associations. High-quality perfusion-deficit maps from CTA can illuminate neural dependents of clinical deficits in the critical pre-interventional period. Our approach enables quantification of neuroanatomical susceptibility to ischaemic threat pre-intervention, with wide applications in predictive and prescriptive modelling in cerebrovascular disorders.

References

1. Feigin, V. L. et al. World Stroke Organization (WSO): Global Stroke Fact Sheet 2022. *International Journal of Stroke* 17, 18–29 (2022).
2. Tangwiriysakul, C. et al. Framework to Generate Perfusion Map from CT and CTA Images in Patients with Acute Ischemic Stroke: A Longitudinal and Cross-Sectional Study. in 154–162 (2024). doi:10.1007/978-3-031-76160-7_15.
3. Katyal, A. & Maimonides Bhaskar, S. M. Value of pre-intervention CT perfusion imaging in acute ischemic stroke prognosis. *Diagnostic and Interventional Radiology* 27, 774–785 (2021).

4. Khandelwal, N. CT perfusion in acute stroke. *Indian Journal of Radiology and Imaging* 18, 281–286 (2008).
5. Brott, T. et al. Measurements of acute cerebral infarction: a clinical examination scale. *Stroke* 20, 864–870 (1989).
6. Chalos, V. et al. National Institutes of Health Stroke Scale. *Stroke* 51, 282–290 (2020).
7. Pombo, G. et al. Deep Variational Lesion-Deficit Mapping. (2023).
8. Mah, Y.-H., Husain, M., Rees, G. & Nachev, P. Human brain lesion-deficit inference remapped. *Brain* 137, 2522–2531 (2014).
9. Xu, T., Jha, A. & Nachev, P. The dimensionalities of lesion-deficit mapping. *Neuropsychologia* 115, 134–141 (2018).
10. Vernet, M., Quentin, R., Chanes, L., Mitsumasu, A. & Valero-Cabré, A. Frontal eye field, where art thou? Anatomy, function, and non-invasive manipulation of frontal regions involved in eye movements and associated cognitive operations. *Front Integr Neurosci* 8, (2014).
11. Brotchie, P. R. et al. Head Position Modulates Activity in the Human Parietal Eye Fields. *Neuroimage* 18, 178–184 (2003).
12. Li, Y. et al. Fast high-resolution metabolic imaging of acute stroke with 3D magnetic resonance spectroscopy. *Brain* 143, 3225–3233 (2020).
13. Cao, J., Ball, I. K., Cassidy, B. & Rae, C. D. Functional conductivity imaging: quantitative mapping of brain activity. *Phys Eng Sci Med* 47, 1723–1738 (2024).
14. Moriconi, S. et al. VTrails: Inferring Vessels with Geodesic Connectivity Trees. in 672–684 (2017). doi:10.1007/978-3-319-59050-9_53.
15. Moriconi, S. et al. Inference of Cerebrovascular Topology With Geodesic Minimum Spanning Trees. *IEEE Trans Med Imaging* 38, 225–239 (2019).
16. Hope, T. M. H. et al. Principal component analysis-based latent-space dimensionality under-estimation, with uncorrelated latent variables. *Brain* 147, e14–e16 (2024).
17. Halai, A. D., Woollams, A. M. & Lambon Ralph, M. A. Using principal component analysis to capture individual differences within a unified neuropsychological model of chronic post-stroke aphasia: Revealing the unique neural correlates of speech fluency, phonology and semantics. *Cortex* 86, 275–289 (2017).

18. Kwon, H. G. et al. Dentatorubrothalamic tract in human brain: diffusion tensor tractography study. *Neuroradiology* 53, 787–791 (2011).
19. Glickstein, M., May, J. G. & Mercier, B. E. Corticopontine projection in the macaque: The distribution of labelled cortical cells after large injections of horseradish peroxidase in the pontine nuclei. *Journal of Comparative Neurology* 235, 343–359 (1985).
20. Morecraft, R. J. et al. New Corticopontine Connections in the Primate Brain: Contralateral Projections From the Arm/Hand Area of the Precentral Motor Region. *Front Neuroanat* 12, (2018).
21. Ferris, J. K. et al. Modulation of the Association Between Corticospinal Tract Damage and Outcome After Stroke by White Matter Hyperintensities. *Neurology* 102, (2024).
22. Hamilton, R. H., Chrysikou, E. G. & Coslett, B. Mechanisms of aphasia recovery after stroke and the role of noninvasive brain stimulation. *Brain Lang* 118, 40–50 (2011).
23. Binder, J. R. The Wernicke area. *Neurology* 85, 2170–2175 (2015).
24. Nasios, G., Dardiotis, E. & Messinis, L. From Broca and Wernicke to the Neuromodulation Era: Insights of Brain Language Networks for Neurorehabilitation. *Behavioural Neurology* 2019, 1–10 (2019).
25. Nishitani, N., Schürmann, M., Amunts, K. & Hari, R. Broca's Region: From Action to Language. *Physiology* 20, 60–69 (2005).
26. Gummadavelli, A. et al. Thalamic stimulation to improve level of consciousness after seizures: Evaluation of electrophysiology and behavior. *Epilepsia* 56, 114–124 (2015).
27. Min, B.-K. A thalamic reticular networking model of consciousness. *Theor Biol Med Model* 7, 10 (2010).
28. PENFIELD, W. EPILEPSY AND SURGICAL THERAPY. *Arch Neurol Psychiatry* 36, 449 (1936).
29. Cavanna, A. E. The Precuneus and Consciousness. *CNS Spectr* 12, 545–552 (2007).
30. Busler, J. N., Yanes, J. A., Bird, R. T., Reid, M. A. & Robinson, J. L. Differential functional patterns of the human posterior cingulate cortex during activation and deactivation: a meta-analytic connectivity model. *Exp Brain Res* 237, 2367–2385 (2019).

31. Leech, R. & Sharp, D. J. The role of the posterior cingulate cortex in cognition and disease. *Brain* 137, 12–32 (2014).
32. Luo, C. et al. Middle longitudinal fascicle is associated with semantic processing deficits in primary progressive aphasia. *Neuroimage Clin* 25, 102115 (2020).
33. Menjot de Champfleury, N. et al. Middle longitudinal fasciculus delineation within language pathways: A diffusion tensor imaging study in human. *Eur J Radiol* 82, 151–157 (2013).
34. Makris, N. & Pandya, D. N. The extreme capsule in humans and rethinking of the language circuitry. *Brain Struct Funct* 213, 343–358 (2009).
35. Rolheiser, T., Stamatakis, E. A. & Tyler, L. K. Dynamic Processing in the Human Language System: Synergy between the Arcuate Fascicle and Extreme Capsule. *The Journal of Neuroscience* 31, 16949–16957 (2011).
36. Koops, E. A., Haykal, S. & van Dijk, P. Macrostructural Changes of the Acoustic Radiation in Humans with Hearing Loss and Tinnitus Revealed with Fixel-Based Analysis. *The Journal of Neuroscience* 41, 3958–3965 (2021).
37. Almairac, F., Herbet, G., Moritz-Gasser, S., de Champfleury, N. M. & Duffau, H. The left inferior fronto-occipital fasciculus subserves language semantics: a multilevel lesion study. *Brain Struct Funct* 220, 1983–1995 (2015).
38. Ryu, H. & Park, C.-H. Structural Characteristic of the Arcuate Fasciculus in Patients with Fluent Aphasia Following Intracranial Hemorrhage: A Diffusion Tensor Tractography Study. *Brain Sci* 10, 280 (2020).
39. Maffei, C., Sarubbo, S. & Jovicich, J. A Missing Connection: A Review of the Macrostructural Anatomy and Tractography of the Acoustic Radiation. *Front Neuroanat* 13, (2019).
40. Amiez, C. & Petrides, M. Anatomical organization of the eye fields in the human and non-human primate frontal cortex. *Prog Neurobiol* 89, 220–230 (2009).
41. Husain, M., Parton, A., Hodgson, T. L., Mort, D. & Rees, G. Self-control during response conflict by human supplementary eye field. *Nat Neurosci* 6, 117–118 (2003).
42. Nachev, P., Kennard, C. & Husain, M. Functional role of the supplementary and pre-supplementary motor areas. *Nat Rev Neurosci* 9, 856–869 (2008).
43. Coiner, B. et al. Functional neuroanatomy of the human eye movement network: a review and atlas. *Brain Struct Funct* 224, 2603–2617 (2019).

44. Herbet, G., Zemmoura, I. & Duffau, H. Functional Anatomy of the Inferior Longitudinal Fasciculus: From Historical Reports to Current Hypotheses. *Front Neuroanat* 12, (2018).
45. Schmahmann, J. D. & Pandya, D. N. Superior Longitudinal Fasciculus and Arcuate Fasciculus. in *Fiber Pathways of the Brain* 393–408 (Oxford University Press New York, 2006). doi:10.1093/acprof:oso/9780195104233.003.0013.
46. Martino, J., Brogna, C., Robles, S. G., Vergani, F. & Duffau, H. Anatomic dissection of the inferior fronto-occipital fasciculus revisited in the lights of brain stimulation data☆. *Cortex* 46, 691–699 (2010).
47. Latini, F. et al. New Insights Into the Anatomy, Connectivity and Clinical Implications of the Middle Longitudinal Fasciculus. *Front Neuroanat* 14, (2021).
48. Smallwood, J. et al. The default modes of reading: modulation of posterior cingulate and medial prefrontal cortex connectivity associated with comprehension and task focus while reading. *Front Hum Neurosci* 7, (2013).
49. Mashal, N., Vishne, T. & Laor, N. The role of the precuneus in metaphor comprehension: evidence from an fMRI study in people with schizophrenia and healthy participants. *Front Hum Neurosci* 8, (2014).
50. Wahl, M. et al. The Human Thalamus Processes Syntactic and Semantic Language Violations. *Neuron* 59, 695–707 (2008).
51. Gordon, N. Speech, language, and the cerebellum. *Int J Lang Commun Disord* 31, 359–367 (1996).
52. Geva, S. et al. Right cerebral motor areas that support accurate speech production following damage to cerebellar speech areas. *Neuroimage Clin* 32, 102820 (2021).
53. Neophytou, K., Wiley, R., Litovsky, C., Tsapkini, K. & Rapp, B. The right hemisphere's capacity for language: evidence from primary progressive aphasia. *Cerebral Cortex* 33, 9971–9985 (2023).
54. Coffman, K. A., Dum, R. P. & Strick, P. L. Cerebellar vermis is a target of projections from the motor areas in the cerebral cortex. *Proceedings of the National Academy of Sciences* 108, 16068–16073 (2011).

55. Kessner, S. S. et al. Somatosensory Deficits After Ischemic Stroke. *Stroke* 50, 1116–1123 (2019).
56. Balslev, D. & Odoj, B. Distorted gaze direction input to attentional priority map in spatial neglect. *Neuropsychologia* 131, 119–128 (2019).
57. Japee, S., Holiday, K., Satyshur, M. D., Mukai, I. & Ungerleider, L. G. A role of right middle frontal gyrus in reorienting of attention: a case study. *Front Syst Neurosci* 9, (2015).
58. Moore, M. J., Vancleef, K., Shalev, N., Husain, M. & Demeyere, N. When neglect is neglected: NIHSS observational measure lacks sensitivity in identifying post-stroke unilateral neglect. *J Neurol Neurosurg Psychiatry* 90, 1070–1071 (2019).
59. Basagni, B. et al. Critical issue on the extinction and inattention subtest of NIHSS scale: an analysis on post-acute stroke patients attending inpatient rehabilitation. *BMC Neurol* 21, 475 (2021).
60. Uddin, L. Q., Nomi, J. S., Hébert-Seropian, B., Ghaziri, J. & Boucher, O. Structure and Function of the Human Insula. *Journal of Clinical Neurophysiology* 34, 300–306 (2017).
61. Dodds, C. M., Morein-Zamir, S. & Robbins, T. W. Dissociating Inhibition, Attention, and Response Control in the Frontoparietal Network Using Functional Magnetic Resonance Imaging. *Cerebral Cortex* 21, 1155–1165 (2011).
62. Mort, D. J. The anatomy of visual neglect. *Brain* 126, 1986–1997 (2003).
63. Cavanna, A. E. & Trimble, M. R. The precuneus: a review of its functional anatomy and behavioural correlates. *Brain* 129, 564–583 (2006).
64. Dadario, N. B. & Sughrue, M. E. The functional role of the precuneus. *Brain* 146, 3598–3607 (2023).
65. Verdon, V., Schwartz, S., Lovblad, K.-O., Hauert, C.-A. & Vuilleumier, P. Neuroanatomy of hemispatial neglect and its functional components: a study using voxel-based lesion-symptom mapping. *Brain* 133, 880–894 (2010).
66. Ben-Shabat, E., Matyas, T. A., Pell, G. S., Brodtmann, A. & Carey, L. M. The Right Supramarginal Gyrus Is Important for Proprioception in Healthy and Stroke-Affected Participants: A Functional MRI Study. *Front Neurol* 6, (2015).
67. Chilvers, M., Low, T., Rajashekar, D. & Dukelow, S. White matter disconnection impacts proprioception post-stroke. *PLoS One* 19, e0310312 (2024).

68. Benarroch, E. E., Cutsforth-Gregory, J. K. & Flemming, K. D. Sensory System. in Mayo Clinic Medical Neurosciences (eds. Benarroch, E. E., Cutsforth-Gregory, J. K. & Flemming, K. D.) 209–248 (Oxford University Press, 2017). doi:10.1093/med/9780190209407.003.0007.
69. Park, S. H. et al. Integration of visual feedback and motor learning: Corticospinal vs. corticobulbar pathway. *Hum Mov Sci* 58, 88–96 (2018).
70. Ding, L. et al. Lesion Network Mapping for Neurological Deficit in Acute Ischemic Stroke. *Ann Neurol* 94, 572–584 (2023).
71. Onder, H., Albayrak, L. & Polat, H. Frontal lobe ischemic stroke presenting with peripheral type facial palsy: A crucial diagnostic challenge in emergency practice. *Turk J Emerg Med* 17, 112–114 (2017).
72. Bonkhoff, A. K. et al. Acute ischaemic stroke alters the brain's preference for distinct dynamic connectivity states. *Brain* 143, 1525–1540 (2020).
73. Bonkhoff, A. K. et al. Generative lesion pattern decomposition of cognitive impairment after stroke. *Brain Commun* 3, (2021).
74. Bonkhoff, A. K. et al. Outcome after acute ischemic stroke is linked to sex-specific lesion patterns. *Nat Commun* 12, 3289 (2021).
75. Giles, D. et al. Individualized prescriptive inference in ischaemic stroke. (2023).
76. Giles, D. et al. InterSynth: A Semi-Synthetic Framework for Benchmarking Prescriptive Inference from Observational Data. in 172–188 (2024). doi:10.1007/978-3-031-47679-2_13.
77. Ito, H., Kanno, I., Takahashi, K., Ibaraki, M. & Miura, S. Regional distribution of human cerebral vascular mean transit time measured by positron emission tomography. *Neuroimage* 19, 1163–1169 (2003).
78. Zavaglia, M., Malherbe, C., Schlaadt, S., Nachev, P. & Hilgetag, C. C. Ground-truth validation of uni- and multivariate lesion inference approaches. *Brain Commun* 6, (2024).
79. Dargazanli, C. et al. Mechanical Thrombectomy for Minor and Mild Stroke Patients Harboring Large Vessel Occlusion in the Anterior Circulation. *Stroke* 48, 3274–3281 (2017).
80. Laurencin, C. et al. Thrombolysis for Acute Minor Stroke: Outcome and Barriers to Management. *Cerebrovascular Diseases* 40, 3–9 (2015).

81. Brudfors, M., Balbastre, Y., Flandin, G., Nachev, P. & Ashburner, J. Flexible Bayesian Modelling for Nonlinear Image Registration . in *Medical Image Computing and Computer Assisted Intervention — MICCAI 2020* (eds. Martel, A. L. et al.) 253–263 (Springer International Publishing, Lima, Peru, 2020). doi:10.1007/978-3-030-59716-0.
82. Perona, P. & Malik, J. Scale-space and edge detection using anisotropic diffusion. *IEEE Trans Pattern Anal Mach Intell* 12, 629–639 (1990).
83. Lee, T. C., Kashyap, R. L. & Chu, C. N. Building Skeleton Models via 3-D Medial Surface Axis Thinning Algorithms. *CVGIP: Graphical Models and Image Processing* 56, 462–478 (1994).
84. Konukoglu, E. et al. A Recursive Anisotropic Fast Marching Approach to Reaction Diffusion Equation: Application to Tumor Growth Modeling. in 687–699 (2007). doi:10.1007/978-3-540-73273-0_57.
85. Benmansour, F. & Cohen, L. D. Tubular Structure Segmentation Based on Minimal Path Method and Anisotropic Enhancement. *Int J Comput Vis* 92, 192–210 (2011).
86. Yeh, F.-C. Population-based tract-to-region connectome of the human brain and its hierarchical topology. *Nat Commun* 13, 4933 (2022).

Methods

Dataset

We retrospectively enrolled a cohort of patients admitted to the stroke unit at King's College Hospital between 2015 to 2019, consisting of 2110 patients with a paired CT and CTA on admission. From that cohort, we excluded those with (1) incomplete NIHSS sub-score ($n=64$), (2) failure on visual inspection of adequate co-registration between CT and CTA ($n=134$), and (3) presence of a mild deficit as indexed by total NIHSS ≤ 4 ($n=519$)^{79,80}, see details in the Supplementary Fig 1. The clinical pathway involves obtaining an NIHSS immediately on initial assessment, followed by CT and CTA typically within 30 minutes. Inclusion criteria were met by 1393 patients (mean [SD] age = 69.89 [15.70] years, female = 645, male = 748). The patients' data from King's College Hospital were accessed according to ethics protocol 20/ES/0005, approved by the East of Scotland Research Ethics Service

Data pre-processing and estimation of computed perfusion map

Fig 1 summarises the data pre-processing step and the estimation of computed perfusion map. Each patient's CT and CTA were co-registered, and non-linearly normalized with CTseg (<https://github.com/WCHN/CTseg>) into MNI space by obtaining the parameters from the CT and applying the estimated deformation field to both images, resliced at 1x1x1 mm resolution⁸¹. The normalized images were then processed using the first two steps of VTrails^{14,15}: (1) digital subtraction image pre-processing and (2) vascular contrast enhancement and seeds detection. In step 1, we created a digitally subtracted image (DSA) by subtraction of CT from CTA, followed by rescaling of the intensity distribution to the interval 0 to 1. In step 2, we extracted seed points from the vascular contrast-enhanced version of the DSA^{14,15}. In this step, we first applied a gradient anisotropic filter to the DSA image as in Perona-Malik⁸². This filter suppresses noise while preserving the edges of the vascular structure to produce a filtered DSA image or a vesselness speed potential (VSP). We then binarised the VSP image to segment the vessels using the VTrails default threshold of 0.2¹⁴ (<https://vtrails.github.io/VTrailsToolkit/>). The binarised VSP was then converted into a skeleton image using itkBinaryThinningImageFilter3D⁸³ from the Insight Toolkit (ITK;

www.itk.org). This step uses a 3D decision tree-based algorithm to thin the binary image to a skeleton representing the centreline of the vascular structure. Every voxel within the skeleton having a value in the VSP image greater than the 75th percentile (VTrails' default parameter) was defined as a seed point, yielding a Seed image. Finally, any seed point located inside the cerebral venous map was removed.

A fast-marching algorithm was applied to the DSA and Seed images to estimate the vascular time-of-arrival at each voxel, with the seed points as the source and the DSA as the speed potential matrix⁸⁴. The fast-marching algorithm is a special case of Dijkstra's algorithm⁸⁵. It computes a minimal geodesic path between two points within an anisotropic medium by minimising an energy function weighted by the medium, in our case the speed potential matrix^{14,85}. We chose seed points located along the centreline of the arterial lumen because the velocity profile is highest along the centreline and monotonically decreases away from it in the orthogonal plane. Our seed points thus represent the source of oxygenated blood to neighbouring brain areas. Using the intensity of the DSA as the speed potential matrix assumes that oxygenation will be faster where the vasculature is denser. Under these constraints, the algorithm calculates, for each voxel outside the skeleton, the fastest propagation time from a skeletal seed point. The resulting voxel-wise image of time-of-arrival comprises the CPM. Since the DSA was normalised between 0 to 1, the CPM is unitless. A higher voxel value reflects a longer time taken for blood to perfuse the location, hence a higher risk of ischemia at that voxel. Fig-1 depicts all steps to estimate the CPM from CT and CTA. We ran our scripts using MATLAB2020a on an Intel(R) Core(TM) i9-9900K computer. For each subject, it took 539 seconds (SD=49 seconds) to process CT/CTA images, run VTrails and estimate the CPM. After that, all CPMs and resliced them into a 2x2x2 mm image.

Perfusion-deficit mapping

We employed deep variational lesion-deficit mapping (DLM), a mechanism for spatial inference, introduced by Pombo et al.⁷, based on the variational autoencoder (VAE). The model was fitted to 1393 patients: 90% for training, and 10% equally for validation and calibration.

DLM here learns a latent representation (Z) that explains the joint distribution of CPM and NIHSS sub-scores under the biologically plausible assumption—implicit in all lesion-deficit mapping—that the observed deficit is the dot product between the perfusion map and the inferred neural substrate. The DLM encoder is a convolutional neural net (CNN) mapping the CPM and paired NIHSS sub-score to a 50-dimensional latent representation Z . The DLM decoder is a CNN that maps Z to the inferred neural substrate, in the same space as the CPM, along with a reconstruction of the CPM. The NIHSS sub-score is also reconstructed, as the dot product between the inferred neural substrate and the original CPM. This is the inductive bias, introduced in Pombo et al.⁷, that lesion-deficit mapping in general foundationally presupposes. The inset in Fig 2 depicts the relationship between the underlying neural substrate and the CPM.

Implementation of Perfusion-DLM

Fig 2 depicts the Perfusion-DLM models implemented in our study. A 5-channel matrix comprised of the computed perfusion map (CPM), X, Y, and Z coordinates and the NIHSS sub-score was fed into the network.

The encoder φ comprises seven layers. The first six involve the following sequence of operations: (1) a 3D convolution, with a 3x3x3 kernel and a stride of 1x1x1; (2) batch normalisation; (3) a nonlinear component-wise activation function (the Gaussian Error Linear Unit function or GELU); and (4) another 3D convolution, with a 2x2x2 kernel and a stride of 2x2x2, so that the spatial dimensions are halved after each layer. The number of output channels in each layer is 5, 16, 32, 64, 128, 256, respectively. The seventh layer is a fully connected layer consisting of 100 output channels and 2048 input channels. The first 50 are the mean of the posterior distribution of Z , and the second 50 are its standard deviation.

The decoder consists of two branches, γ and θ , which act on separate halves of the 50-dimensional latent representation. The first branch, γ , maps the first 25 dimensions of Z to the latent substrate; the second branch, θ , maps the second 25 dimensions to the reconstruction of the CPM. Both branches start with a fully connected layer that maps 25 dimensions to 256x2x2x2. The subsequent layers effectively replicate the encoder, but in

reverse. The loss function is the variational lower bound on the log likelihood of the joint distribution of the CPM and the NIHSS sub-score, comprising the sum of (1) the KL-divergence; (2) the L2-loss between the reconstructed and original CPM; and (3) the L2-loss between the reconstructed and original NIHSS sub-score, see Fig 2.

We minimise the variational lower bound using ADAM, with a learning rate of 1e-4 and a weight decay of 1e-5. The networks were trained for a maximum of 4,000 epochs, with a batch size of ten, on an NVIDIA-DGX-A100. The model weights were saved after each epoch, and after 4,000 epochs we kept the model that best estimates the NIHSS sub-score.

Statistics

The outputs from Perfusion-DLM networks are (1) inferred neural substrate, (2) reconstructed perfusion map, and (3) reconstructed NIHSS sub-score. As described in Pombo et al.⁷, we binarized the neural substrate to determine deficit-associated neural areas by performing calibration on 5% of the data (70 participants), independently selected for each NIHSS sub-score. We searched for the best threshold between a range of 90.5 to 99.5 percentile. At each iteration, we calculated the predicted NIHSS sub-score by multiplying the binarized substrate with a perfusion map at each subject and averaged across all 70 subjects from the calibration dataset. The critical level was selected from at the iteration with the highest accuracy.

Tissue-specific inferred substrates

Since the physiological effects of damage to white and grey matter are plausibly different, each derived substrate was segmented into gray and white matter components based on the CTseg white-matter and gray-matter template⁸¹.

For each white matter substrate, we created a tractography of constituent fibre bundles using a white matter bundle atlas⁸⁶. A fibre tract was considered involved if at least two white matter voxels were located within 2 mm of the tract. Note that we performed a sensitivity analysis across eight conditions (2, 4, 6, 8, 10, 12, 14, and 16 WM voxels) and found no notable differences among them. Therefore, two WM voxels were chosen as the

criterion for a disrupted WM tract in our study (see Supplementary Table 14). For each bundle, we calculated a magnitude of disruption [MDU], defined as the proportion of disrupted tracts relative to the total streamlines that make up for a given specific white matter tract. Unless otherwise specified, all derived substrates in this paper were visualized using SurfICE (<https://www.nitrc.org/projects/surface/>).

Report summary

Further information on research design is available in the Nature Portfolio Reporting Summary linked to this article.

Code availability

All code can be found at the following links: <https://github.com/WCHN/CTseg> (data registration), <https://vtrails.github.io/VTrailsToolkit/> (computed perfusion map), https://github.com/guilherme-pombo/vae_lesion_deficit (Deep Variational Lesion-Deficit mapping).

Data availability

The data that support this project are not publicly available due to the ethical policy governing the use of our clinical data does not allow data sharing.

Acknowledgement

CT, PB, SM, PW, JR, RG, PN, SO, and MJC are supported by the Wellcome Trust (WT213038/Z/18/Z). MJC, and SO are also supported by the Wellcome/EPSRC Centre for Medical Engineering (WT203148/Z/16/Z), and the InnovateUK-funded London AI Centre for Value-based Healthcare. YM is supported by an MRC Clinical Academic Research Partnership grant (MR/T005351/1). PN is also supported by the UCLH NIHR Biomedical Research Centre.

Author contributions

Conceptualisation, CT, PN, MJC. Methodology and investigation, CT, PB, GP, SM, ME, PW, YM, JR, RG, PN, MJC. Resources, PW, YM, SO, PN, MJC. Writing CT, PN, MJC. Visualisation

and analysis, CT, YM, PN, MJC. Supervision PN, MJC. All authors revised and approved the paper.

Competing interests

MJC, SO, and PN are founding shareholders in Hologen, a deep generative modelling company. The remaining authors declare no competing interests. A fast-marching algorithm is a part of technologies undergoing patent filing (PCT/GB2020/052368, PCT/GB2021/050349) owned by King's College London.

Main Figures

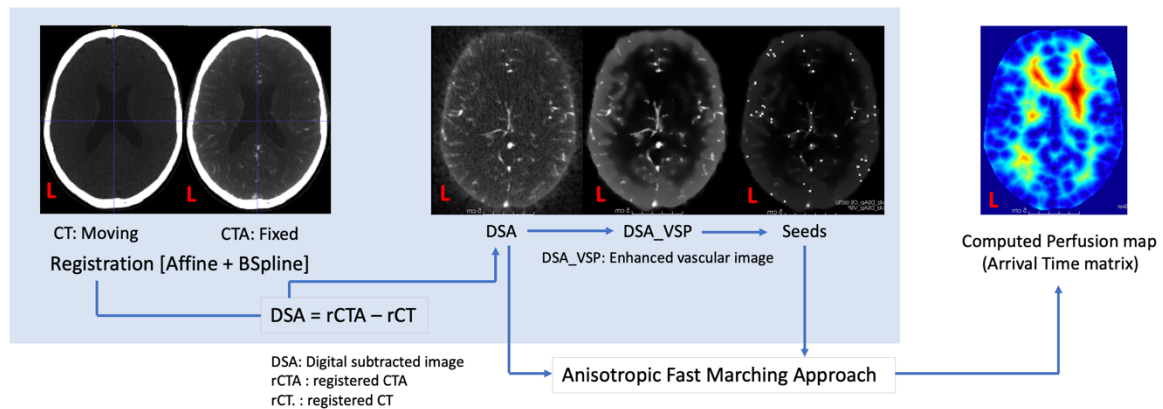


Figure 1: Preprocessing steps and the estimation of the computed perfusion map (CPM).

Note that: The left side of the brain is shown to the left.

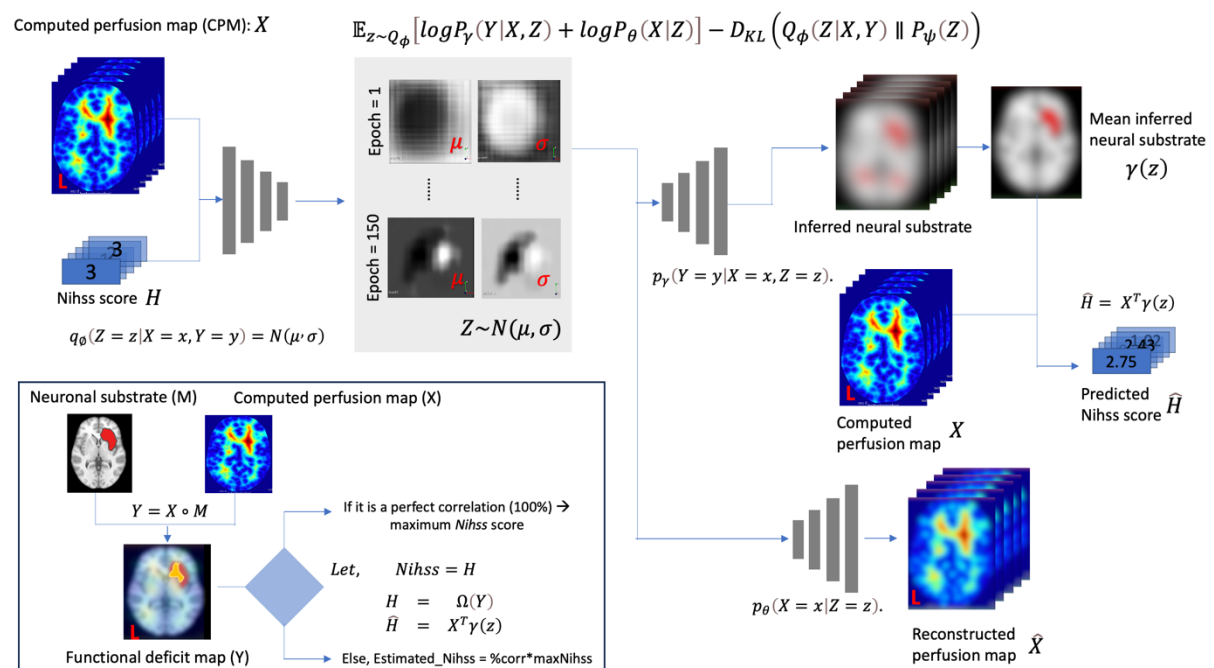


Figure 2: The networks.

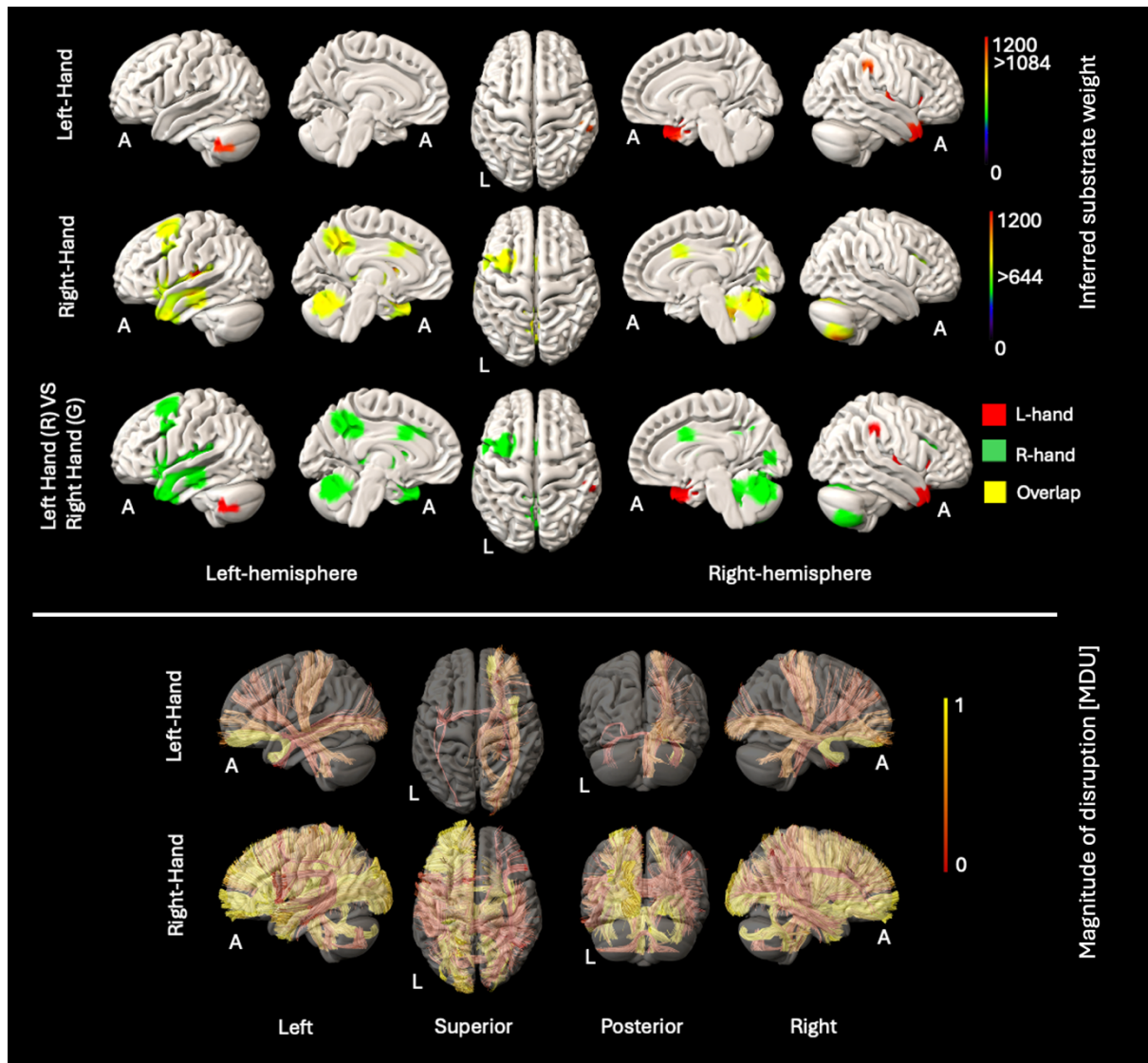


Figure 3: The top panel shows GM perfusion-deficit maps for the left hand (top row), right hand (middle row), and their overlap (bottom row). In the top two rows, the colour bar indicates the strength of association between each brain area and the NIHSS left hand and the NIHSS right hand scores, respectively. Voxels with weights exceeding 1084 (for the left hand) and 644 (for the right hand) are considered significant. In the bottom row, inferred GM substrates are marked in red for the left hand, green for the right hand, and yellow for their overlap. The bottom panel shows disrupted WM tracts for the left hand (top row) and the right hand (bottom row), with the colour bar indicating normalized magnitude of disruption, scaled from 0 to 1 [MDU: Magnitude disruption unit].

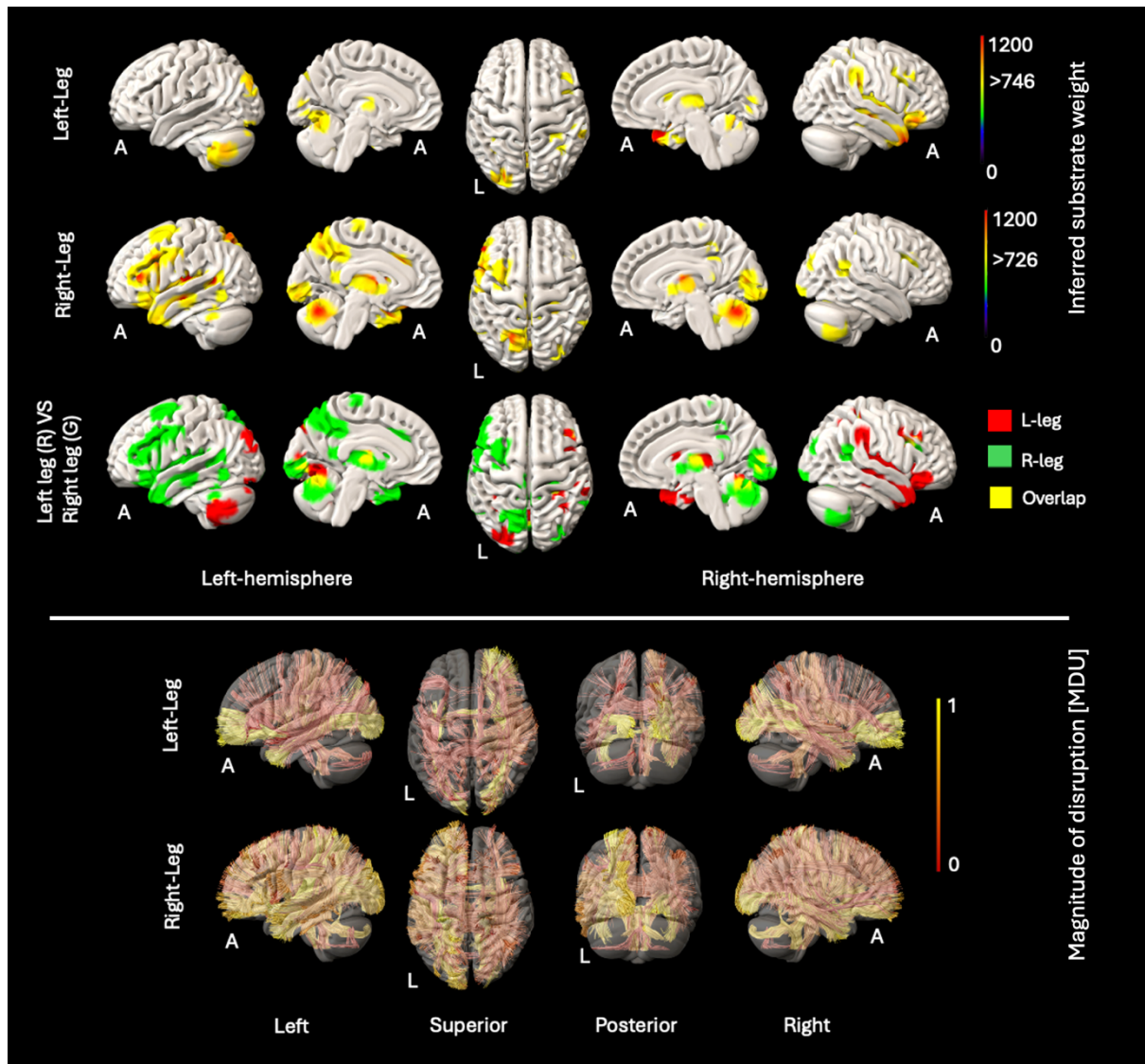


Figure 4: The top panel shows GM perfusion-deficit maps for the left leg (top row), right leg (middle row), and their overlap (bottom row). In the top two rows, the colour bar indicates the strength of association between each brain area and the NIHSS left leg and the NIHSS right leg scores, respectively. Voxels with weights exceeding 746 (for the left leg) and 726 (for the right leg) are considered significant. In the bottom row, inferred GM substrates are marked in red for the left leg, green for the right leg, and yellow for their overlap. The bottom panel shows disrupted WM tracts for the left leg (top row) and the right leg (bottom row), with the colour bar indicating normalized magnitude of disruption, scaled from 0 to 1 [MDU: Magnitude disruption unit].

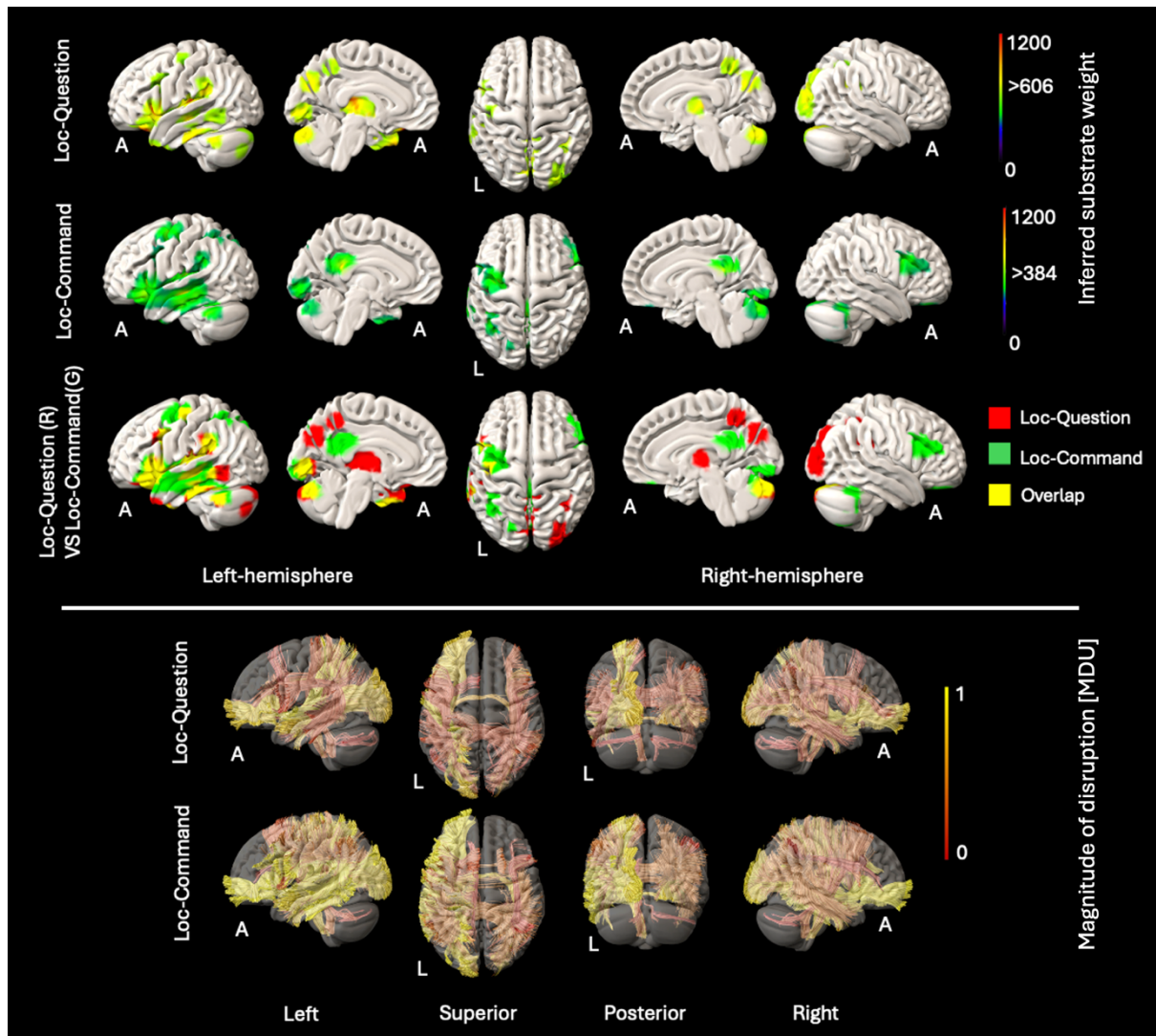


Figure 5: The top panel shows GM perfusion-deficit maps for loc-question (top row), loc-command (middle row), and their overlap (bottom row). In the top two rows, the colour bar indicates the strength of association between each brain area and the NIHSS loc-question and the NIHSS loc-command scores, respectively. Voxels with weights exceeding 606 (for loc-question) and 384 (for loc-command) are considered significant. In the bottom row, inferred GM substrates are marked in red for loc-question, green for loc-command, and yellow for their overlap. The bottom panel shows disrupted WM tracts for loc-question (top row) and loc-command (bottom row), with the colour bar indicating normalized magnitude of disruption, scaled from 0 to 1 [MDU: Magnitude disruption unit].

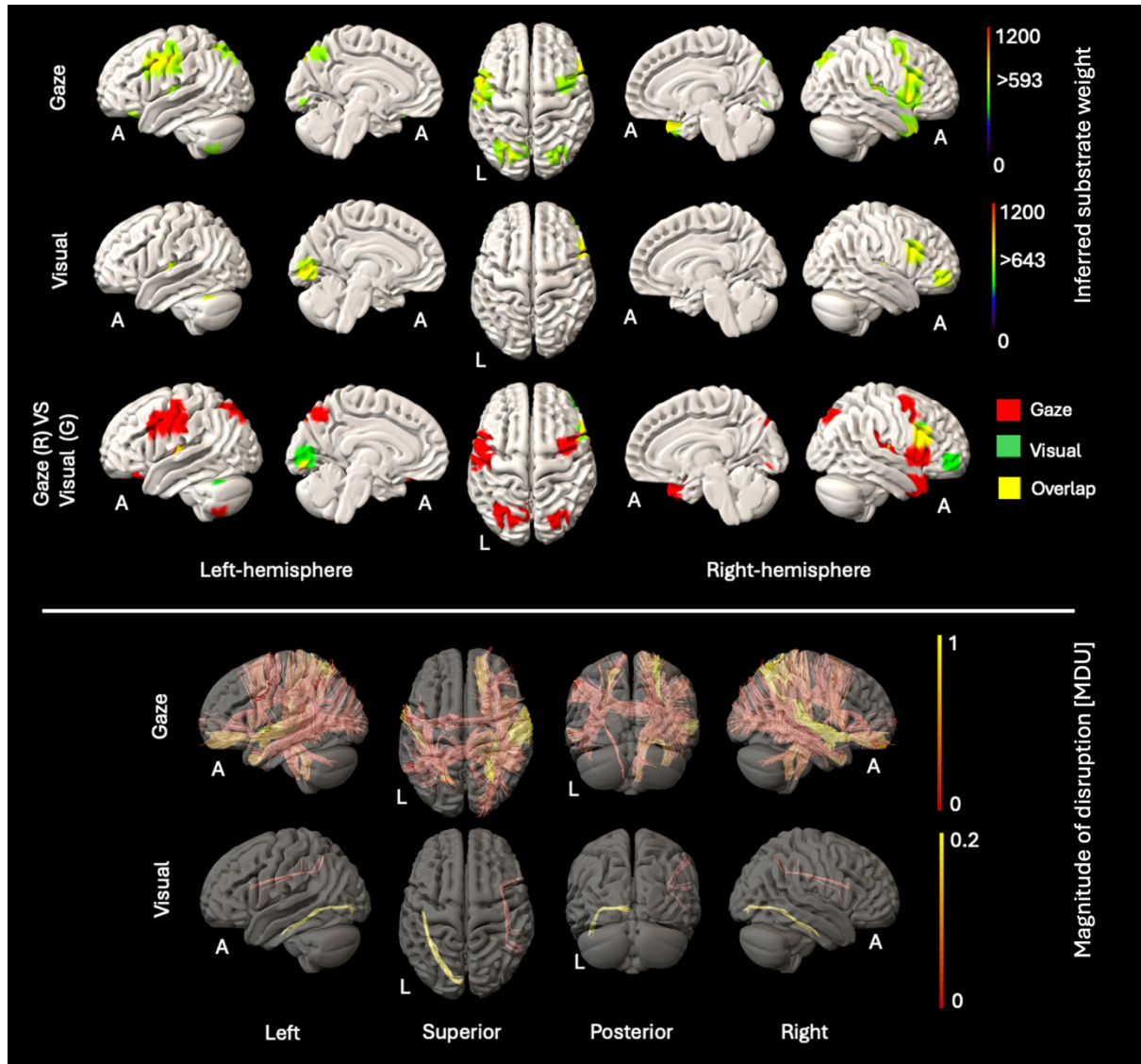


Figure 6: The top panel shows GM perfusion-deficit maps for gaze (top row), visual (middle row), and their overlap (bottom row). In the top two rows, the colour bar indicates the strength of association between each brain area and the NIHSS gaze and the NIHSS visual scores, respectively. Voxels with weights exceeding 593 (for gaze) and 643 (for visual) are considered significant. In the bottom row, inferred GM substrates are marked in red for gaze, green for visual, and yellow for their overlap. The bottom panel shows disrupted WM tracts for gaze (top row) and visual (bottom row), with the colour bar indicating normalized magnitude of disruption, scaled from 0 to 1 [MDU: Magnitude disruption unit] for gaze, and scaled from 0 to 0.2 [MDU] for visual.

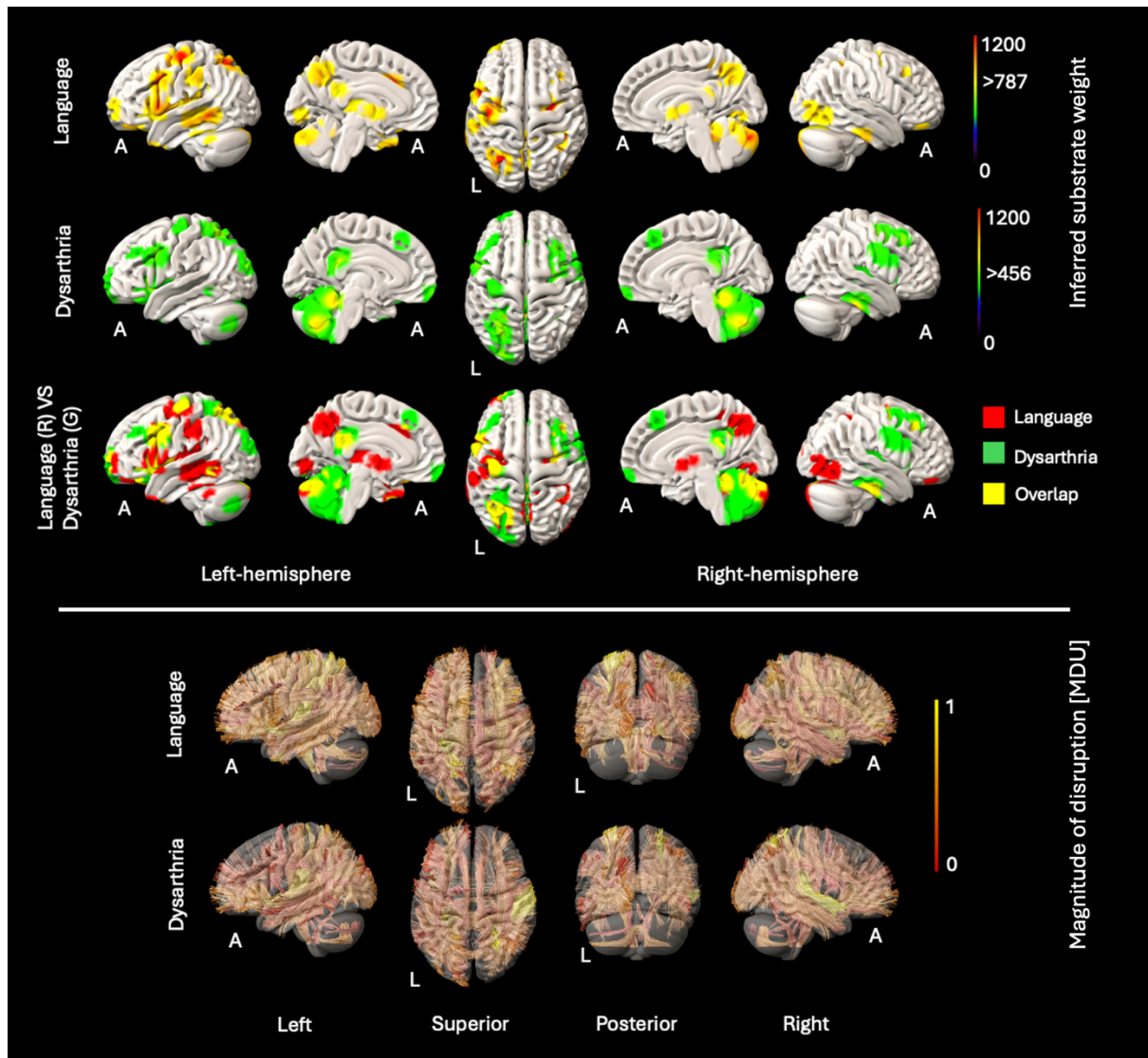


Figure 7: The top panel shows GM perfusion-deficit maps for language (top row), dysarthria (middle row), and their overlap (bottom row). In the top two rows, the colour bar indicates the strength of association between each brain area and the NIHSS language and the NIHSS dysarthria scores, respectively. Voxels with weights exceeding 787 (for language) and 456 (for dysarthria) are considered significant. In the bottom row, inferred GM substrates are marked in red for language, green for dysarthria, and yellow for their overlap. The bottom panel shows disrupted WM tracts for language (top row) and dysarthria (bottom row), with the colour bar indicating normalized magnitude of disruption, scaled from 0 to 1 [MDU: Magnitude disruption unit].

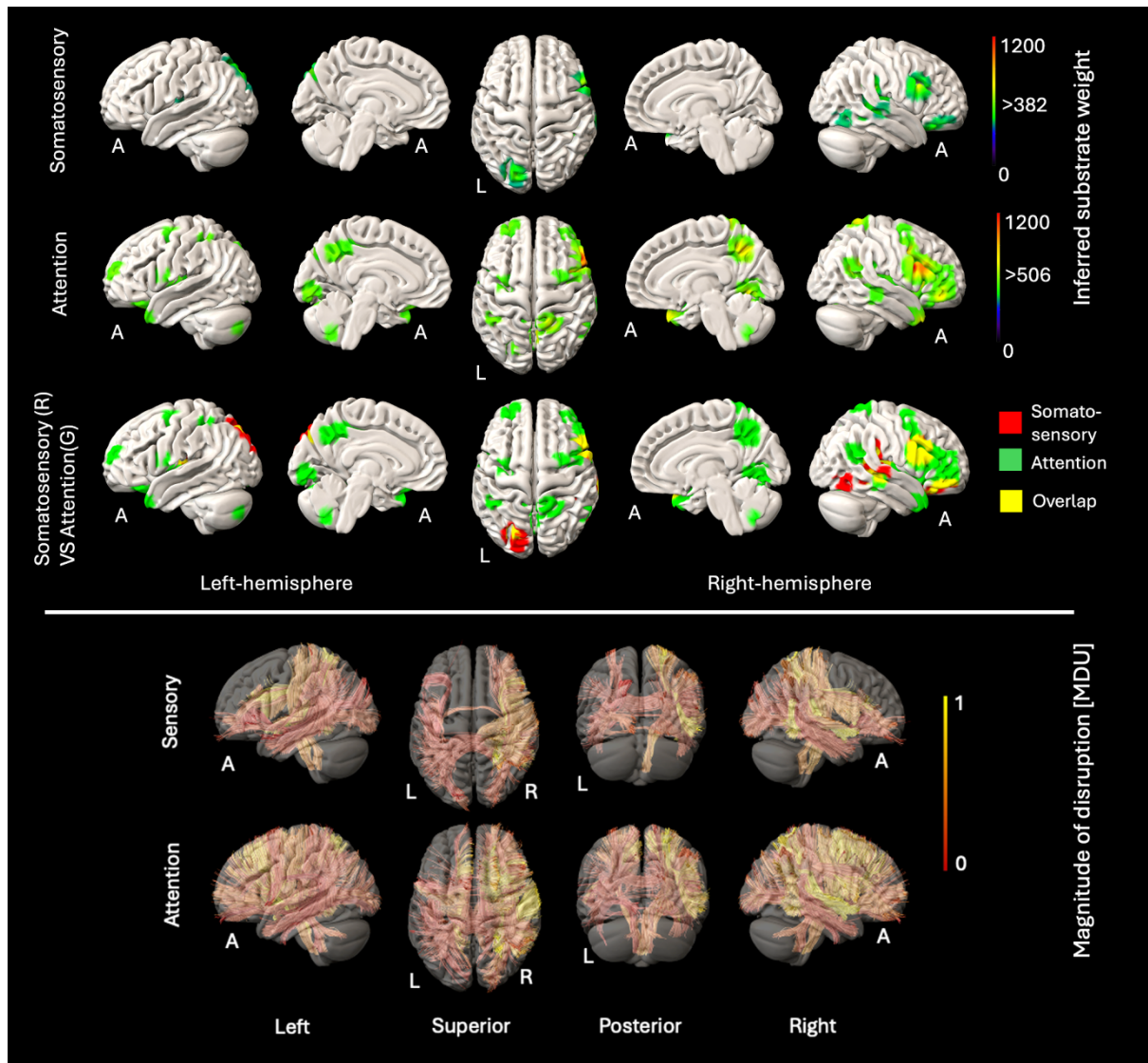


Figure 8: The top panel shows GM perfusion-deficit maps for somatosensory (top row), attention (middle row), and their overlap (bottom row). In the top two rows, the colour bar indicates the strength of association between each brain area and the NIHSS somatosensory and the NIHSS attention scores, respectively. Voxels with weights exceeding 382 (for somatosensory) and 506 (for attention) are considered significant. In the bottom row, inferred GM substrates are marked in red for somatosensory, green for attention, and yellow for their overlap. The bottom panel shows disrupted WM tracts for somatosensory (top row) and attention (bottom row), with the colour bar indicating normalized magnitude of disruption, scaled from 0 to 1 [MDU: Magnitude disruption unit].